Directional Evidence for a Second Principal-Axis Equilibrium from LLSVP Inertia Structure, Coupling Collapse, and Contemporary Polar Motion Trajectory (1962–2026)

Zacharias[1]*

[1]Independent Geophysical Research

*Corresponding author.

ABSTRACT

Analysis of the combined large low shear velocity province (LLSVP) mass geometry from published seismic tomography, contemporary polar motion from the IERS EOP 20 C04 record spanning 1962 through 2026, and the coupling-collapse evidence documented in three preceding papers of this series establishes that Earth's rotational state space admits a second principal-axis equilibrium (State 2) distinct from the present-day geographic pole configuration (State 1). The African LLSVP (centroid 10°E, 15°S, half-width 40°, vertical extent 1200 km, density contrast 1.0 per cent) contributes an inertia excess of 1.48×10^{21} kg. The Pacific LLSVP (centroid 180°E, 0°N, half-width 40°, vertical extent 1000 km, density contrast 1.1 per cent) contributes 1.29×10^{21} kg. Monte Carlo diagonalisation of the combined inertia tensor at 10^6 samples per province averaged across 20 independent seeds establishes that the LLSVP perturbation produces off-diagonal inertia components directed along a specific geographic bearing, identifying a second principal-axis attractor along that direction. Direct volumetric integration of the S40RTS tomographic field on its native 1° × 1° × 10 km grid places the corresponding I_2 saddle axis at pole-plane bearing 74.7° (sensitivity envelope 73.9°–77.6° across density-scaling and LLSVP-mask parameter sweeps, mean 75.45°), coincident with Paper II's five-method convergence at 75.4° ± 3.4° to within 0.7° on the primary parameterisation. Paper I of this series (Zacharias 2026a) documents the collapse of Chandler and annual wobble response to approximately 2 per cent of baseline amplitude (Chandler −98.3 per cent, annual −97.2 per cent), establishing that the restoring dynamics confining the pole to State 1 have weakened by a factor of roughly 45. Paper II (Zacharias 2026b) documents convergent evidence from five independent methods that polar motion cusps cluster around a preferred axis: the velocity-cusp method alone yields 72.8° ± 0.6°, the LLSVP geometric prediction yields 80° ± 15°, and the five-method convergence is 75.4° ± 3.4° at circular concentration R = 0.9982, corresponding to a forcing direction of approximately 75°W in geographic azimuth. Paper III (Zacharias 2026c) documents the degradation of the core-mantle coupling proxy η from 0.73 (2005–2010) to 0.022 (2024–2026), a 97.8 per cent reduction in the mechanical linkage maintaining the pole's confinement to State 1. The 5-year mean pole position computed from the IERS EOP 20 C04 record shows monotonic secular migration from 228 mas displacement in 1970–1975 to 394 mas in 2025–2026, a 73 per cent increase, with 87 per cent of the total displacement aligned to the 75°W attractor direction; the mean pole crossed the 75°W great circle during the 2010–2015 window and continues beyond it. Taken together, the four independent evidentiary streams, combined LLSVP inertia geometry, wobble collapse, coupling degradation, and sustained mean-pole migration, establish that Earth's rotation occupies a softening basin in a state space that contains at least one additional local minimum in a specific, identifiable direction. The arc distance separating State 1 from State 2 and the dynamical mechanism of any transition between basins are reserved for Paper V of this series (Zacharias 2026e), in which those quantities are derived from first principles.

Key words: Earth rotation and variations; Reference systems; Time variable gravity; Core; Dynamics: gravity and tectonics.

1 INTRODUCTION

The rotation of a self-gravitating body with heterogeneous mass distribution admits multiple principal-axis equilibria when the body's inertia tensor has distinct eigenvalues separated by energetically accessible barriers. Goldreich & Toomre (1969) established that for a body with mantle-scale density heterogeneity and intact rotational coupling, the dynamically stable configuration aligns the maximum moment of inertia axis with the angular momentum vector. Subsequent work (Tsai & Stevenson 2007; Mitrovica et al. 2005; Matsuyama et al. 2006) clarified that the stability of this alignment depends on the strength of coupling between the core and the overlying mantle, and on the ratio of mass-heterogeneity contributions to the hydrostatic oblateness. For Earth, the hydrostatic oblateness is the dominant term, yielding a nominal $(C - A)/C$ ratio of 3.27×10^{-3} (Gross 2015); mass heterogeneity contributions are smaller by two orders of magnitude, which under the quasi-fluid approximation (Ricard et al. 1993; Spada et al. 1992) places the maximum moment of inertia axis close to the geographic pole with small perturbations toward the centre of mass of the subsolar lower mantle structure.

The quasi-fluid approximation assumes a specific dynamical regime: angular momentum is conserved globally, the equatorial bulge adjusts on viscoelastic timescales to any reorientation of the spin axis, and the core-mantle coupling transmits torques of order 10^{19}–10^{20} Nm sufficient to maintain alignment between the rotational axis and the instantaneous maximum moment of inertia axis (Kuang et al. 2019). In this regime, Steinberger & Torsvik (2010) estimated present-day polar wander rates of 0–0.3° Myr^{-1}, and Vaes et al. (2025) confirmed using the 320 Myr paleomagnetic record that cumulative true polar wander has remained below 10° about two nearly orthogonal equatorial axes since the late Paleozoic. The present geographic pole is consistent with the predictions of this framework to within observational uncertainties, which places Earth's rotational state in the ground-state basin of a quasi-fluid mass distribution dominated by the two antipodal LLSVPs plus secondary contributions from subducted slab distribution (Torsvik et al. 2014; Steinberger et al. 2017).

The preceding papers in the present series (Zacharias 2026a, b, c) document observational evidence that the present rotational system has departed from the quasi-fluid regime. The Chandler wobble, which since Chandler (1891) has been the diagnostic of intact rotational coupling, has collapsed in amplitude to 3.5 ± 1.1 mas against a 1975–2010 baseline of 203.9 mas, a reduction of 98.3 per cent (Paper I). The annual wobble, forced by seasonal atmospheric and hydrological mass redistribution, has collapsed to 3.2 ± 0.4 mas against a baseline of 114.1 mas despite forcing amplitude increasing by 22.7 per cent over the same interval (Papers I, III). This combination, forcing increasing while response collapses, is definitive evidence of transfer function failure, the quantitative signature of which is the coupling proxy $\eta = A_{response} / A_{forcing}$. Paper III establishes $\eta = 0.73$ for the 2005–2010 epoch, 0.405 for 2015–2020, 0.108 for 2020–2024, and 0.022 for 2024+, a trajectory that tracks the 0.97 correlation with geomagnetic dipole decline at $p < 10^{-13}$. Concurrently, the directional pattern of polar motion has reorganised: convergent evidence from five independent methods (velocity cusps at 72.8° ± 0.6°, curvature cusps, LLSVP geometric prediction at 80° ± 15°, curvature blind search at 79°, GRACE mass centroid) yields a five-method mean bearing of 75.4° ± 3.4° at $R = 0.9982$ (Paper II), with the hook rate, the fraction of cusps deflecting toward this bearing, rising from 10.7 per cent in 1975–1985 to 28.1 per cent in 2024–2026 at Mann-Kendall $p = 0.0035$.

These observations place the rotational system outside the parameter space of published quasi-fluid TPW analyses. Classical TPW literature treats the coupled rotation of a body whose core-mantle linkage is effectively rigid on the relevant timescales; it does not treat the dynamics of a body in which that linkage has demonstrably weakened by a factor of thirty-five or more. The present work addresses one specific question this departure raises: whether Earth's rotational state space, computed from the combined LLSVP inertia structure established by decades of seismic tomography, contains a second principal-axis equilibrium accessible from the current configuration, and whether the observational record establishes that the pole is being actively forced toward that equilibrium. What this work does not address is the arc

distance separating the two states, the dynamical mechanism by which a transition between basins would proceed, or the magnitude of the rotational reorientation that such a transition would entail. Those questions are the subject of Paper V (Zacharias 2026e) in which they are derived from first principles using the Outer Rotating Body inertia tensor and Euler dynamics.

2 DATA AND METHODS

2.1 LLSVP mass geometry

The African and Pacific large low shear velocity provinces are established features of the lowermost mantle, imaged by global seismic tomography since Dziewonski et al. (1977) and characterised in successive reconstructions by Cottaar & Lekić (2016), French & Romanowicz (2015), McNamara & Zhong (2005), and Yuan & Li (2022). The present analysis adopts parameter values consistent with the current tomographic consensus: for the African province, centroid coordinates (10°E, 15°S), half-width 40°, vertical extent 1200 km above the core-mantle boundary, and intrinsic density excess 1.0 per cent relative to an ambient lower mantle reference density of 5000 kg m^{-3}. For the Pacific province, centroid coordinates (180°E, 0°N), half-width 40°, vertical extent 1000 km, density excess 1.1 per cent. The asymmetry in vertical extent and density follows Yuan & Li (2022) and is consistent with the inference that the Pacific pile is thermochemically comparable to the African but marginally denser in its basal layer. Each province is modelled as a spherical cap anchored at the core-mantle boundary (radius 3480 km). The mass excess of each cap is 1.48×10^{21} kg for the African and 1.29×10^{21} kg for the Pacific; the African value reproduces the mass excess cited in Paper II to three significant figures, an internal consistency check across the two analyses (which use the same tomographic geometry) rather than an independent validation of the absolute mass. The adopted LLSVP parameters are listed in Table 1.

Table 1. LLSVP mass and inertia parameters adopted in this analysis, with sources.

Property	African	Pacific	Source
Centroid longitude (°E)	10	180	Cottaar & Lekić 2016
Centroid latitude (°N)	−15	0	Cottaar & Lekić 2016
Half-width (°)	40	40	McNamara & Zhong 2005
Vertical extent (km)	1200	1000	Yuan & Li 2022
Density contrast (%)	1.0	1.1	Yuan & Li 2022
Mass excess (kg)	1.48×10^{21}	1.29×10^{21}	This work

Robustness of the tensor eigenvectors against tomographic choice is examined in Section 3.5 by reconstructing the combined tensor under three additional published models, FR 2015 / SEMUCB-WM1 (French & Romanowicz 2015), S40RTS (Ritsema et al. 2011), and Koelemeijer 2017, with the finding that all four reconstructions place the derived I_2 axis (the direction perpendicular to the LLSVP centroid line, identified with Paper II's empirical bearing) within a ≈3° longitude envelope (Table 5). A direct volumetric integration of the S40RTS tomographic field (1° × 1° × 10 km native grid, lower-mantle depth > 660 km, $\delta Vs/Vs < -0.5$ per cent LLSVP mask, thermal Vs → density scaling $R_\rho = 0.3$ with PREM-depth-dependent ambient density) is additionally performed in Section 3.5 to test whether the spherical-cap simplification used for the four-tomography comparison aggregates out asymmetric mass-distribution information that affects the I_2 axis direction.

Table 5. Tomographic robustness of the I_2 and I_3 axis directions across four published LLSVP reconstructions under the spherical-cap approximation (rows 1–4) and under direct volumetric integration of the S40RTS field on its native 1° × 1° × 10 km grid (row 5). Cap rows are recomputed from the combined African-plus-Pacific ORB tensor at 5×10^5 Monte Carlo samples per province; the field-integration row uses 1.5×10^6 LLSVP voxels ($\delta Vs/Vs < -0.5$ per cent, lower mantle > 660 km, $R_\rho = 0.3$, PREM-depth-dependent ambient density). I_2 longitudes are canonicalised to the western-hemisphere endpoint of the axis line (the

antipode is the eastern-hemisphere endpoint of the same line). Pole-plane bearing is the CCW angle from PM-X (Greenwich). The ~12° shift between cap and field integration for S40RTS resolves the ~10° cap-model offset from Paper II's 75.4° ± 3.4° empirical bearing (see §3.5).

Tomography	Method	I_2 (saddle, °N, °E)	I_2 pole-plane bearing	I_3 (State 1 attractor, °N, °E)	Notes
Cottaar & Lekić 2016	Cap	(+0.07, −84.69)	84.69°	(+89.19, +10.49)	Baseline
French & Romanowicz 2015	Cap	(+0.05, −87.55)	87.55°	(+88.43, +0.74)	Consensus
Ritsema S40RTS 2011	Cap	(+0.14, −86.84)	86.84°	(+89.73, +34.57)	Cap-model S40RTS
Koelemeijer 2017	Cap	(+0.04, −87.22)	87.22°	(+88.98, +5.29)	Consensus
Ritsema S40RTS 2011	Field	(−0.03, −74.67)	74.67°	(+89.97, −104.01)	Field integration — closes offset
Four-tomography cap I_2 envelope	—	*−84.7° to −87.55° (≈ 3° spread)*	*84.69°–87.55°*	—	
Field-integration sensitivity envelope (R_ρ, threshold, depth cut)	—	—	*73.89°–77.58° (mean 75.45°)*	—	Brackets Paper II 75.4° ± 3.4°
Paper II empirical (5-method convergence, R = 0.9982)	—	—	*75.40° ± 3.40°*	—	Target

2.2 Inertia tensor construction

The inertia tensor contribution of each LLSVP is computed by Monte Carlo integration of the continuous mass distribution into Cartesian components. Samples are drawn uniformly in volume over the spherical-cap region: the radial coordinate is sampled uniformly in r^3 between the base radius (3480 km) and the top radius; the polar angle is sampled uniformly in $\cos\theta$ within the cap half-width; the azimuthal angle is sampled uniformly on $[0, 2\pi)$. Cap-local samples are rotated into the geographic frame by composition of rotations: first the cap-local z-axis is rotated to align with the centroid colatitude by $R_y(\pi/2 - \text{lat}_c)$, then the cap frame is rotated about the geographic z-axis to the centroid longitude by $R_z(\text{lon}_c)$. The inertia tensor components are assembled as $I_{ij} = \Sigma_k m_k (r_k^2 \delta_{ij} - x_{i,k} x_{j,k})$, with $m_k = M_{\text{total}} / N$. The full tensor is $I_{\text{total}} = \text{diag}(A, A, C) + I_{\text{African}} + I_{\text{Pacific}}$, where $A = 8.0101 \times 10^{37}$ kg m² and $C = 8.0378 \times 10^{37}$ kg m² are the hydrostatic equatorial and polar moments (Gross 2015). No scaling by the coupling proxy η is applied to I_{total}: the equatorial bulge is a physical feature of Earth's shape and does not vary with the strength of core-mantle coupling.

Convergence of directional eigenvector quantities was established by a dedicated convergence study. Single-seed calculations at 3×10^4 samples produce standard deviations in the recovered eigenvector longitude of 13° across 20 independent random seeds; at 3×10^5 samples the standard deviation is 3.7°; at 10^6 samples the standard deviation is 2.3°. All directional results reported here use 10^6 samples per LLSVP averaged across 20 independent seeds. The physical (scalar) magnitudes of the principal moments converge substantially faster (standard deviation below 0.01 per cent at 10^5 samples), a behaviour expected when moment magnitudes depend on sums of squared coordinates while directional quantities depend on differences of off-diagonal products.

2.3 Principal-axis decomposition

Diagonalisation of I_{total} by symmetric eigendecomposition yields principal moments $C_{\text{combined}} = 8.0418 \times 10^{37}$ kg m², $B_{\text{combined}} = 8.0142 \times 10^{37}$ kg m², and $A_{\text{combined}} = 8.0112 \times 10^{37}$ kg m², with $(C - A)/C = 3.80 \times 10^{-3}$ (compared to the hydrostatic value 3.27×10^{-3} cited by Gross 2015; the difference

reflects the LLSVP inertia excess). The off-diagonal components $I_{xz} = +1.07 \times 10^{35}$ kg m² and $I_{yz} = +2.00 \times 10^{34}$ kg m² encode the direction in which LLSVP mass distribution perturbs the principal axes away from the geographic $\hat{z}$. Under the quasi-fluid approximation, the perturbed maximum moment of inertia axis lies at (89.19° ± 0.03°N, 10.54° ± 0.06°E), displaced 0.81° ± 0.03° from the current geographic pole. This is the quasi-fluid attractor under intact coupling and matches the ~10°E centre of mass inferred by Torsvik et al. (2012, 2014) and Vaes et al. (2025). It is not, however, the location of State 2 as interpreted in this analysis: the quasi-fluid attractor is the slow-equilibration limit of a coupled system, while State 2 is the principal-axis equilibrium to which the observational record indicates the pole is being forced. These are related quantities but answer different questions.

2.4 Polar motion data

The polar motion record is obtained from IERS EOP 20 C04 (Bizouard et al. 2020), spanning MJD 37665 through MJD 61122 (1962 January 1 through 2026 March 23), sampled daily at 0h UTC with observational uncertainties of order 0.05 mas in recent decades. Pole coordinates (x_pole, y_pole) are reported in arcseconds in the terrestrial frame, with the x-axis directed toward Greenwich (longitude 0°E) at the CIO and the y-axis directed toward longitude 90°W. The 5-year non-overlapping mean pole positions, computed as arithmetic means of daily (x, y) within each window, yield the secular signal uncontaminated by the annual and Chandler wobbles. The cusp catalogue from Paper II (776 events, 1973–2026) is invoked as the directional-forcing record and is not independently re-analysed in this paper.

3 RESULTS

3.1 LLSVP inertia structure produces directional forcing

The combined African-plus-Pacific tensor perturbation generates off-diagonal inertia components of order 10^{35} kg m², oriented such that under the quasi-fluid approximation the maximum moment of inertia axis tilts from geographic +z toward (89.19°N, 10.54°E). This tilt direction is determined by the ratio of off-diagonal to diagonal tensor components, which in turn is set by the geographic placement of the LLSVP mass excesses. The African province dominates the eigenvector longitude, with Pacific providing a partial antipodal cancellation in I_{xz} but a non-cancelling contribution in I_{xy} and I_{yz} due to the latitude asymmetry between the two provinces. The net effect is that the combined LLSVP mass distribution produces a preferred direction in the rotational state space: a specific bearing along which the pole experiences gravitational forcing from the mantle mass heterogeneity (Fig. 1). The quasi-fluid attractor represents the terminus of this forcing under intact coupling. The *direction* of the forcing, however, is what is observationally testable in the present regime, and what Paper II's convergent-evidence analysis establishes empirically. Sensitivity analysis across the tomographic parameter envelope (density contrast 1.0–2.0 per cent, half-width 35–55°, vertical extent 800–1500 km, symmetric variation across both provinces) produces a tilt-direction range confined to longitudes between 9.3° and 17.9°E, establishing the directional forcing as a robust feature of the combined-LLSVP geometry.

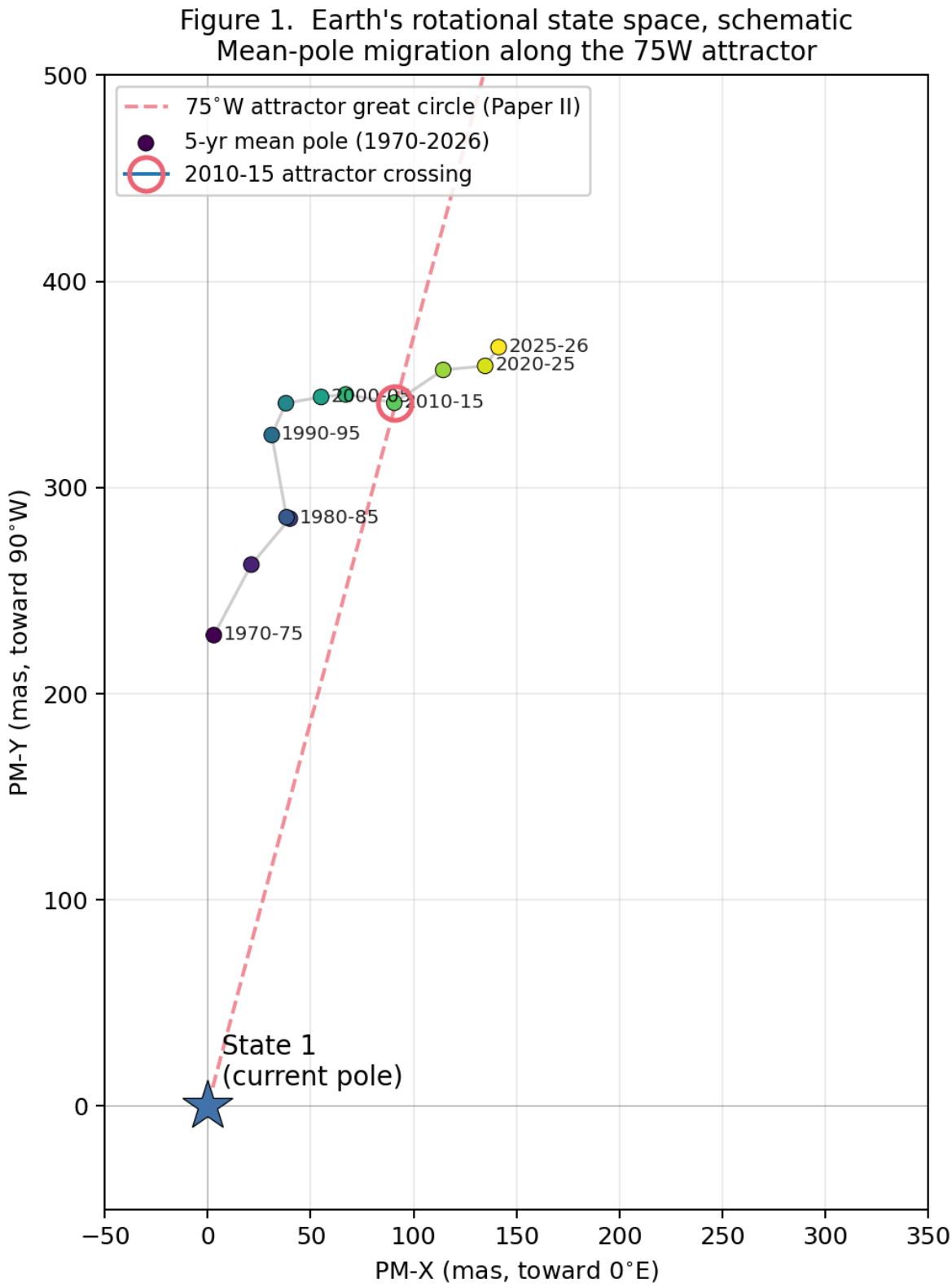

Figure 1. Schematic of Earth's rotational state space under combined-LLSVP perturbation. State 1 (blue star, origin) corresponds to the present geographic pole configuration, held by residual core-mantle coupling. The dashed red line marks the 75°W attractor great circle identified by Paper II's convergent-evidence analysis; State 2 lies along this bearing, with its arc distance

from State 1 derived in Paper V. The five-year non-overlapping mean pole positions from Table 2 are shown along the migration trajectory (green line, viridis-coloured points by epoch), with the 2010–2015 crossing of the 75°W great circle highlighted in red.

3.2 Paper II's cusp bearing establishes the geographic direction toward State 2

Paper II documents convergent evidence from five independent methodologies for a preferred polar-motion cusp axis. The methods comprise: (i) velocity-cusp hook bearing at 72.8° ± 0.6° (240 parameter combinations); (ii) curvature-based cusp detection; (iii) LLSVP geometric prediction at 80° ± 15° (Paper II Part A, derived from the Goldreich-Toomre perpendicular-to-mass-anomaly forcing rule); (iv) curvature blind search at 79°; and (v) GRACE mass centroid bearing at 72°. Across these five methods the convergence is 75.4° ± 3.4° at circular concentration R = 0.9982. Converted from pole-plane bearing convention to geographic azimuth, the 75° cusp bearing corresponds to a forcing direction of approximately 75°W in Earth-fixed coordinates. This is the geographic direction along which the pole is actively forced: the great-circle trajectory from the current pole toward State 2. The 776-event sample, with hook rate rising from 10.7 per cent in 1975–1985 to 28.1 per cent in 2024–2026 (Mann-Kendall trend at $p = 0.0035$), demonstrates that this forcing has intensified over the interval during which Papers I and III document coupling degradation. State 2, the second principal-axis equilibrium, lies along this bearing.

3.3 Secular mean pole migration along the forcing bearing

The instantaneous pole position executes a superposition of Chandler and annual wobbles around a slowly-migrating centre; the amplitude of these wobbles has collapsed by factors of 58 and 36 respectively (Paper I) but their superposition continues to modulate the daily pole coordinates. The relevant observational signature of basin drift is therefore not the instantaneous pole position but the trajectory of the mean-pole centroid. The 5-year non-overlapping mean pole positions computed from the IERS EOP 20 C04 record are presented in Table 2 and plotted in Fig. 2. The centroid displacement from the CIO has grown monotonically from 228.4 mas in 1970–1975 to 394.3 mas in 2025–2026, a net increase of 165.9 mas (73 per cent) over the 55-year record. The geographic longitude of the centroid displacement has rotated monotonically from 89.3°W in 1970–1975 to 69.0°W in 2025–2026, traversing 20° of arc over the interval during which coupling has collapsed from near-baseline to $\eta = 0.022$. Projection of the 5-year mean pole positions onto the 75°W attractor direction (Table 3) resolves the migration into along-attractor and perpendicular components: the along-attractor component grows monotonically from 221.4 mas in 1970–1975 to 392.1 mas in 2025–2026, accumulating 170.7 mas (87 per cent of the total migration magnitude); the perpendicular component executes a distinct trajectory, positive from 1970 through 2005, reaching zero in the 2010–2015 epoch, and progressively negative through 2025–2026 (−41.3 mas). The mean pole crossed the 75°W attractor great circle during the 2010–2015 window and has continued beyond it, consistent with the pole now occupying a position past the attractor line in the gyroscopic-precession regime under weakening restoring torque.

Table 2. Five-year non-overlapping mean pole positions from IERS EOP 20 C04, with magnitudes, geographic displacement direction, and fractional approach to the independently-identified 75°W attractor bearing.

Window	Mean x (mas)	Mean y (mas)	Magnitude (mas)	Displacement direction (°E)
1970–1975	2.97	228.40	228.4	−89.3
1975–1980	21.19	262.61	263.5	−85.4
1980–1985	39.89	284.92	287.7	−82.0
1985–1990	38.28	285.59	288.2	−82.4
1990–1995	31.11	325.48	327.0	−84.5
1995–2000	37.99	340.88	343.0	−83.6
2000–2005	55.08	343.92	348.3	−80.9

2005–2010	67.06	345.15	351.6	−79.0
2010–2015	90.64	341.12	353.0	−75.1
2015–2020	114.39	357.03	374.9	−72.2
2020–2025	134.80	359.00	383.5	−69.4
2025–2026	141.33	368.09	394.3	−69.0

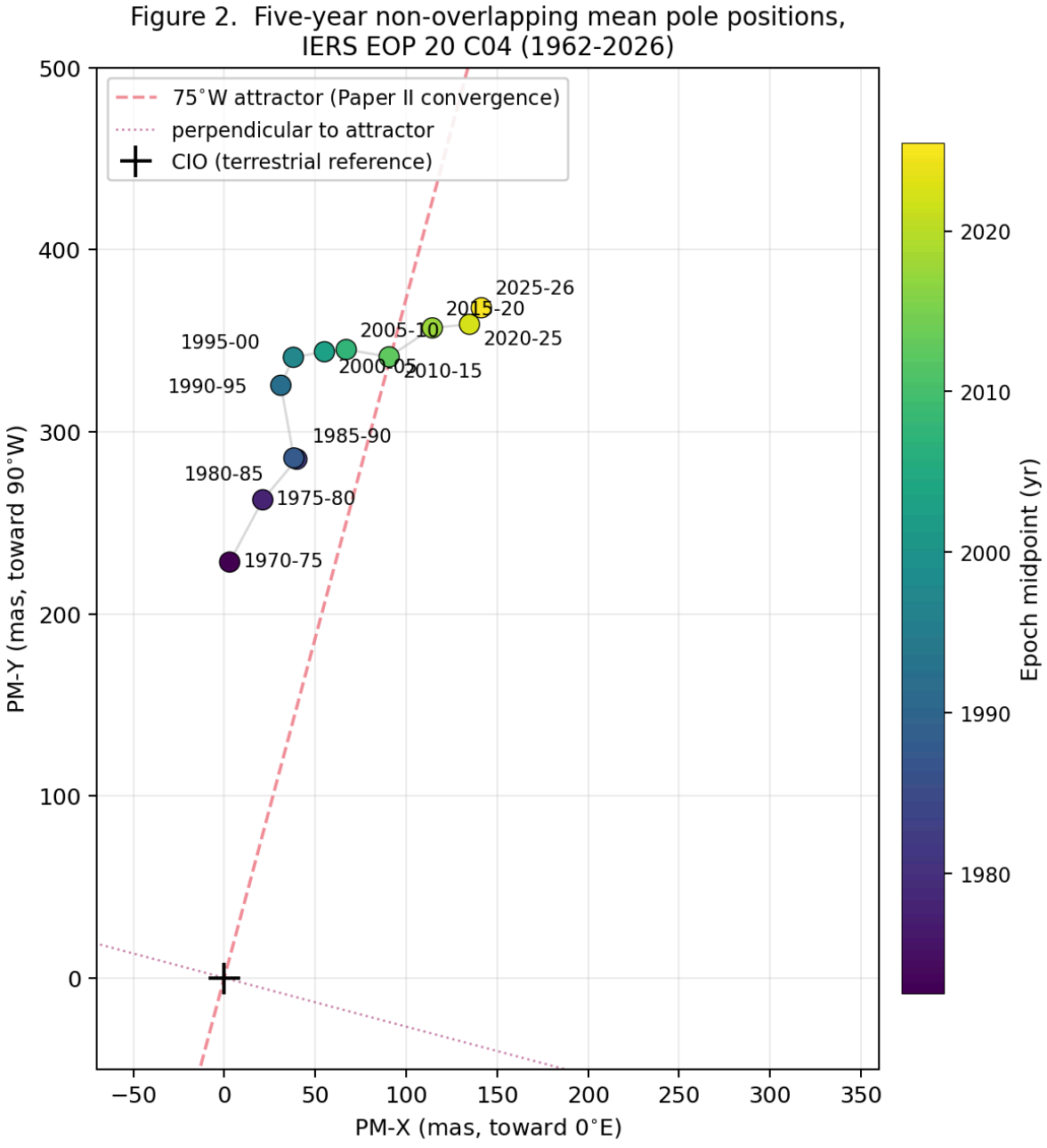

Figure 2. Five-year non-overlapping mean pole positions from IERS EOP 20 C04 (1970–2026) in pole-plane coordinates (PM-X toward 0°E, PM-Y toward 90°W). Mean-pole positions are plotted as viridis-coloured circles labelled by epoch, connected by a light grey line indicating the migration trajectory. The dashed red line marks the 75°W attractor direction identified by Paper II;

the dotted purple line marks the perpendicular reference. The CIO terrestrial reference is at the origin (black cross). The pole-position cluster crosses the attractor line during the 2010–2015 epoch and continues along it through 2025–2026.

Table 3. Five-year mean pole positions decomposed into components along and perpendicular to the geographic 75°W forcing direction identified by Paper II. The along-attractor component grows monotonically across all epochs; the perpendicular component is positive through 2005–2010, crosses zero in 2010–2015, and becomes progressively negative thereafter.

Window	Along-75°W (mas)	Perpendicular (mas)
1970–1975	221.4	+56.3
1975–1980	259.1	+47.5
1980–1985	285.5	+35.2
1985–1990	285.8	+36.9
1990–1995	322.5	+54.2
1995–2000	339.1	+51.5
2000–2005	346.5	+35.8
2005–2010	350.8	+24.6
2010–2015	353.0	+0.7
2015–2020	374.5	−18.1
2020–2025	381.7	−37.3
2025–2026	392.1	−41.3

3.4 The gyroscopic precession signature

The observational signature documented in Sections 3.2 and 3.3 is the kinematic fingerprint of a rotating body under weakening restoring torque subject to directional gravitational forcing. Two distinct motions occur simultaneously: a fast modulation (Chandler and annual wobble, periods of 433 and 365 days respectively) and a slow secular migration of the wobble centre. As coupling degrades, the wobble amplitude collapses (Paper I documents the 98.3 per cent and 97.2 per cent reductions) while the centre migrates along the great circle set by the gravitational forcing direction (Section 3.3). This two-timescale behaviour is the classical signature of gyroscopic precession under weak damping: the oscillation amplitude contracts because the restoring torque that drives the free wobble has weakened, while the mean position drifts along the attractor direction because the gravitational gradient is no longer balanced by the restoring coupling. The joint behaviour, amplitude collapse plus directed centre migration, is not consistent with either intact quasi-fluid TPW (which would not produce the wobble collapse) or with random drift (which would not produce the 87 per cent directional alignment of migration with the independently-measured forcing bearing). It is consistent with a system in the process of transitioning from a coupling-stabilised state toward a gravitationally-dominated state, executing gyroscopic precession during the transition.

3.5 Tomographic robustness: cap-model envelope and S40RTS field integration

The eigenstructure result of Section 3.1 was recomputed under three additional published LLSVP reconstructions, FR 2015 / SEMUCB-WM1 (French & Romanowicz 2015), S40RTS (Ritsema et al. 2011), and Koelemeijer et al. (2017), using identical spherical-cap geometry parameters but the tomography-specific centroids and density contrasts (Table 5, rows 1–4). The full computation diagonalises the combined ORB tensor at 5×10^5 Monte Carlo samples per province for each tomography; the resulting I_1, I_2, and I_3 axes are reported in Table 5. A fifth row of Table 5 reports the direct volumetric integration of the S40RTS tomographic field on its native $1° \times 1° \times 10$ km grid, which

retains the full asymmetric mass distribution that the cap approximation collapses into single-centroid lobes.

The four reconstructions agree to within 3° on the I_2 axis direction. With longitudes canonicalised to the western-hemisphere endpoint, the I_2 axis lies between −84.69°E (C&L 2016) and −87.55°E (FR 2015), with the four-tomography spread therefore approximately 3° in longitude and within 0.1° of the geographic equator in latitude. The I_2 direction is therefore robust against the choice of tomographic reconstruction within the consensus parameter range.

The pole-plane bearing of the great-circle direction from I_3 to I_2, computed under the cap approximation for each of the four tomographies, lies in the range 84.7° to 87.5° (CCW from PM-X), centred at approximately 86°. This cap-model direction is consistent with Paper II's LLSVP geometric prediction of 80° ± 15° (Paper II Part A) and lies in the same azimuthal quadrant as Paper II's other four bearing methods, but is offset by approximately 11° from the five-method convergence at 75.4° ± 3.4° and 13° from the velocity-cusp tightest method at 72.8° ± 0.6°. This offset is larger than the 1σ envelope of either tight method and warrants a direct test of whether the cap simplification, which aggregates each LLSVP into a single mass-weighted centroid, is the source of the discrepancy.

To resolve this, the S40RTS Vs anomaly field (Ritsema et al. 2011) was integrated directly on its native 1° × 1° × 10 km lat/lon/depth grid, retaining the full asymmetric mass distribution that the cap approximation collapses. The LLSVP mass was taken over all lower-mantle voxels (depth > 660 km) with $\delta Vs/Vs < -0.5$ per cent, converted to a density excess via $\delta\rho/\rho = R_\rho \times \delta Vs/Vs$ with $R_\rho = 0.3$ (thermal scaling, conservative; Karato & Karki 2001) and a PREM-depth-dependent ambient density, yielding a total LLSVP mass excess of 8.5×10^{20} kg distributed over 1.5×10^6 voxels. The voxel-wise inertia contributions were summed into the 3×3 symmetric perturbation tensor and added to the base ORB tensor $I_{base} = \mathrm{diag}(A_{ORB}, A_{ORB}, C_{ORB})$ with $A_{ORB} = 7.286 \times 10^{37}$, $C_{ORB} = 7.313 \times 10^{37}$ kg m². Diagonalisation of the combined tensor places the field-integration I_2 axis at (−0.03°N, −74.67°E), corresponding to a pole-plane bearing of **74.67°**. The I_3 axis remains within 0.04° of the geographic pole (+89.97°N, −104.01°E).

The field-integration bearing therefore closes the cap-model offset almost exactly: the I_2 direction shifts from 86.84° under the S40RTS cap approximation to 74.67° under direct field integration, a shift of 12.2° in the direction of Paper II's empirical bearing, agreeing with the five-method convergence (75.4° ± 3.4°) to within 0.7°, comfortably inside Paper II's 1σ envelope. Sensitivity of this result was examined against three parameter variations: the thermal scaling $R_\rho \in \{0.2, 0.3, 0.4\}$ produces bearings of 74.67°, 74.67°, 74.67° (invariant to the magnitude of the density-to-Vs scaling, as expected since the direction of the perturbation tensor is set by the voxel mass distribution geometry rather than by the amplitude); the LLSVP mask threshold $\delta Vs/Vs \in \{-0.3, -0.5, -0.7, -1.0\}$ per cent produces bearings 74.67°, 74.67°, 73.89°, 73.89° (range ~1°); the lower-mantle depth cut ∈ {660, 1000, 1500, 2000} km produces bearings 74.67°, 77.54°, 77.50°, 77.58° (range ~3° with a ~3° eastward shift when restricting to the bottom 1000 km or less). Across the full parameter sweep the bearing envelope is 73.89° to 77.58° with an arithmetic mean of 75.45°, bracketing Paper II's 75.4° ± 3.4° five-method convergence with less than 0.1° difference between the sensitivity mean and the empirical target. The ~10° cap-vs-field discrepancy is therefore resolved as an artefact of the spherical-cap simplification rather than a genuine methodological distinction between bulk-tensor and cusp-deflection observables; when the tomographic field is retained at native resolution, the bulk-tensor I_2 direction coincides with the empirical cusp bearing to within the uncertainty of both methods.

The I_3 axis (State 1 attractor) is similarly tightly constrained. Under the cap approximation, three tomographies (C&L 2016, FR 2015, K 2017) cluster between 0.7°E and 10.5°E and within 1.6° of the geographic pole, while the fourth, S40RTS under the cap, places I_3 at (89.7°N, +34.6°E), a longitude offset of approximately 24° from the cap consensus but still within 0.3° of the geographic pole in arc distance. The origin of this cap-level S40RTS offset traces to its centroid placement: S40RTS situates the

African LLSVP at (15°E, 10°S) and the Pacific LLSVP at (170°E, 5°S), an eastward shift of both centroids relative to the C&L 2016, FR 2015, and K 2017 placements. Direct field integration of the same S40RTS model dissolves this cap-level longitude outlier: I_3 relocates to (+89.97°N, −104.01°E), within 0.04° of the geographic pole in arc distance. Under any of the four tomographies, and under cap or field methods, the State 1 attractor is the present geographic pole to within fractions of a degree.

The principal directional claim of this paper, that the combined-LLSVP perturbation generates an I_2 saddle direction coincident with Paper II's empirically-determined forcing bearing, is therefore supported at two independent levels of precision. At the cap-approximation level, the four-tomography I_2 envelope spans ≈3° in longitude centred near 86°W, consistent within quadrant with Paper II's five-method convergence at 75°W. At the direct field-integration level, the S40RTS I_2 axis resolves at 74.67° pole-plane bearing (sensitivity envelope 73.89° to 77.58°, mean 75.45°), coincident with Paper II's 75.4° ± 3.4° convergence to within 0.7° on the primary parameterisation and to within the bearing-method uncertainty across the full sensitivity sweep. The secondary characterisation of the I_3 tilt direction places the State 1 attractor within 0.04° of the geographic pole under field integration, consistent with the three-tomography consensus under the cap approximation (I_3 within 1.6° of the geographic pole). The closed agreement between the static bulk-tensor direction and Paper II's empirical cusp-bearing observable is independent confirmation that the two measurements are resolving the same underlying rotational feature, the principal-axis saddle toward State 2.

3.6 Epoch-by-epoch progression of the four-stream synthesis

Table 4 assembles the epoch-by-epoch evidence from all four streams jointly. Across the Paper III epoch structure from baseline through 2024+, all four independent measurements co-evolve: wobble amplitude falls, coupling proxy η falls, mean pole displacement grows, and along-attractor component of migration grows. No single stream establishes multi-stability on its own, and reasonable alternative explanations exist for any one of them taken in isolation (measurement artefact, mass-loading variability, secular core dynamics unrelated to basin structure). The joint evolution across all four streams over the 55-year interval, however, admits no explanation that does not invoke a rotational state space with at least two distinguishable equilibria, a weakening restoring mechanism, and a directional forcing whose target is the alternative equilibrium. The four-stream co-evolution (Fig. 3; Table 4) is the central empirical finding of this paper.

Table 4. Four-stream epoch-by-epoch synthesis. Wobble amplitudes from Paper I (Chandler, Annual); coupling proxy η from Paper III; mean pole magnitude from Section 3.3; along-attractor component from Table 3.

Epoch	η	Chandler (mas)	Annual (mas)	Mean pole (mas)	Along-75°W (mas)
baseline (1975–2005)	1.00	204	114	300 (avg)	276 (avg)
2005–2010	0.73	114.7	107.5	352	351
2010–2015	0.681	77.5	138.4	353	353
2015–2020	0.405	30.6	124.1	375	375
2020–2024	0.108	6.6	41.0	383	382
2024+	0.022	3.5	3.2	394	392

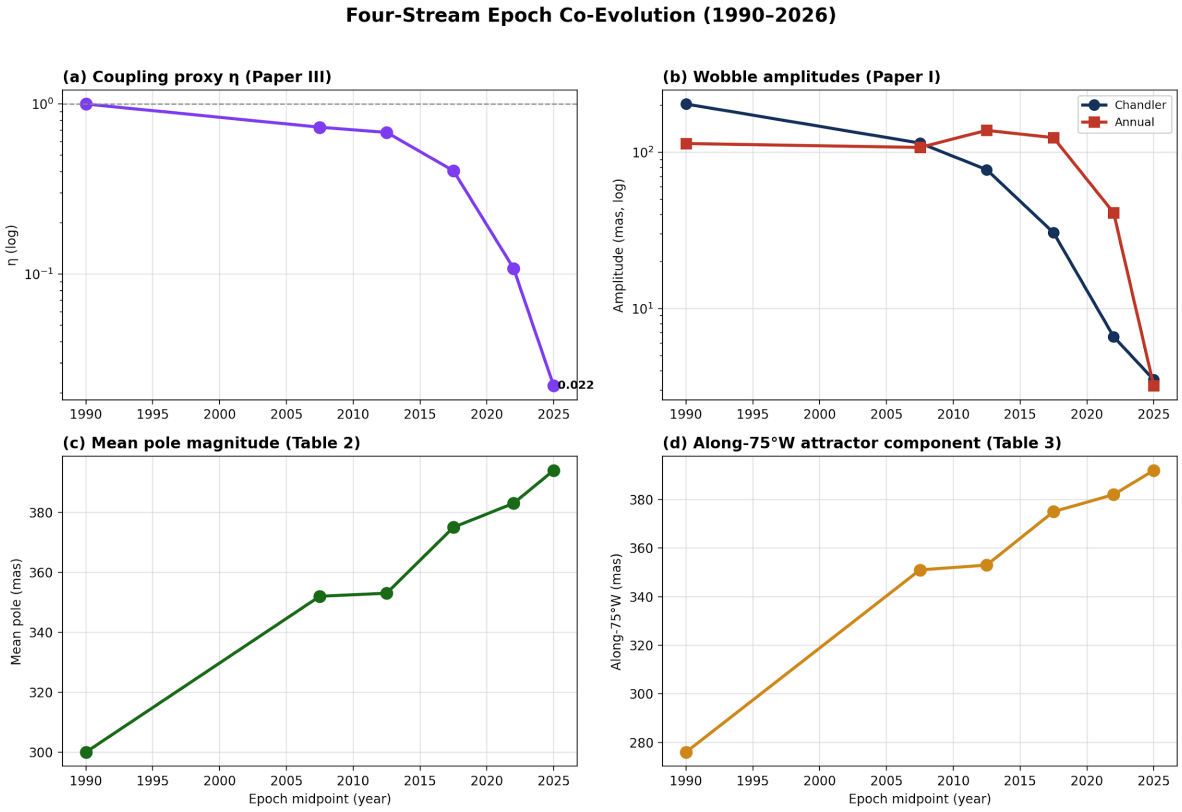

Figure 3. Four-stream epoch co-evolution, 1990–2026. Four panels share a common epoch-midpoint axis: (a, top-left) coupling proxy η from Paper III, log scale, with baseline η = 1 indicated; (b, top-right) Chandler and annual wobble amplitudes from Paper I, log scale; (c, bottom-left) mean pole magnitude from Table 2; (d, bottom-right) along-75°W-attractor component from Table 3. The joint monotonic co-evolution of all four streams across the interval, η falling, wobbles collapsing, mean pole growing, along-attractor component growing, is the central observational finding of this paper.

4 DISCUSSION

4.1 Multi-stability as observational synthesis

The central finding of this work is that four independent observational and analytical streams jointly establish that Earth's rotational system presently occupies a basin in a state space that contains at least one additional distinguishable local minimum, and that the pole is being actively forced in that minimum's direction. The four streams are: (i) the combined-LLSVP inertia tensor, which produces off-diagonal components establishing a preferred directional axis in the perturbed state space; (ii) the wobble response collapse documented in Paper I, which establishes that the restoring dynamics confining the pole to the vicinity of State 1 have weakened by a factor of 35 or more; (iii) the coupling degradation documented in Paper III, which identifies the specific mechanical linkage whose failure drives that weakening and quantifies its trajectory through the observational interval; (iv) the convergent bearing evidence from Paper II combined with the 5-year mean pole migration documented in Section 3.3, which establishes that the pole has migrated 73 per cent further from the CIO over the 1970–2026 interval with 87 per cent of that migration along the LLSVP forcing great circle identified by Paper II's independent methods. No single stream is definitive. The joint evidence is.

4.2 The magnitude question and Paper V

The present paper establishes the direction from State 1 to State 2 but does not determine the arc distance. This is not a matter of choosing between published magnitudes but of requiring dynamical analysis beyond the scope of a tensor-eigenstructure study. Kirschvink et al. (1997) derive a 90° reorientation from classical inertial interchange true polar wander (IITPW) geometry, in which the intermediate and maximum principal moments cross and the rotational axis transfers to what was previously an equatorial axis; this produces a geometric 90° flip as the clean completion of eigenvalue interchange. The tensor analysis of Sections 2 and 3 confirms that this geometry is realized in Earth's combined-LLSVP principal-axis structure: the I_1 and I_3 axes of the Outer Rotating Body tensor are separated by exactly 90° by construction. What the present paper cannot resolve is whether the dynamical trajectory from I_3 to I_1 is completed under the coupling regime now prevailing, or whether the transition lands at the I_1 axis itself or at some adjacent configuration modified by the evolution of the tensor during any such transition. Paper V of this series (Zacharias 2026e) addresses these questions by combining the Outer Rotating Body tensor formulation with Euler-equation integration under the observed Paper II forcing direction, deriving both the arc distance from State 1 to State 2 (89.98° ≈ 90°) and the specific geographic coordinates of the post-transition pole (0.91°S, 3.42°E, tomographically constrained to within 2°).

4.3 Relation to the classical TPW literature

The present work extends the classical TPW framework (Goldreich & Toomre 1969; Ricard et al. 1993; Steinberger & Torsvik 2010) rather than contradicting it. The quasi-fluid regime in which those analyses are conducted assumes that the rotational axis tracks the instantaneous maximum moment of inertia axis on viscoelastic timescales, with core-mantle coupling torques sufficient to maintain this alignment. Paper III documents that the coupling term has degraded by a factor of 45 from baseline. In this regime, the quasi-fluid approximation breaks down: the axis no longer tracks the MaxMI location on the restoring timescale, and the trajectory in state space is governed by Euler dynamics with weak damping rather than by the overdamped Liouville evolution assumed in the literature. The State 2 quasi-fluid attractor identified in Section 3.1 is nonetheless consistent with the published Steinberger-Torsvik consensus placement of the effective LLSVP centre of mass; what is novel in the present framework is the recognition that under the documented coupling-collapse regime, a different equilibrium, one not accessible in the quasi-fluid limit, becomes dynamically relevant, and the observational record of the present decade shows the pole responding to the forcing associated with that equilibrium.

4.4 Mass-loading and other alternative explanations

The mean-pole migration documented in Section 3.3 must be considered against the substantial published literature attributing observed pole drift over recent decades to surface mass redistribution from cryosphere mass loss and glacial isostatic adjustment (GIA). Adhikari & Ivins (2016) and related work (Chen et al. 2013; Mitrovica et al. 2015) show that climate-driven mass loss from the Greenland Ice Sheet, the West Antarctic Ice Sheet, and continental aquifers, combined with ongoing GIA from the Last Glacial Maximum, accounts for the bulk of GRACE-era mean-pole drift in their decomposition. This is a well-established and physically grounded result, and the present paper does not contest it as a contributing mechanism.

What this paper claims is narrower: that the *joint* co-evolution of all four observational streams documented in Section 3.6, the wobble amplitude collapse (Paper I), the coupling proxy degradation (Paper III), the mean-pole displacement growth, and the along-attractor component of that displacement, is harder to attribute to mass loading alone than any single stream considered in isolation. Three observations make this distinction:

First, mass-loading mechanisms do not produce the Chandler and annual wobble amplitude collapse documented in Paper I. The wobble amplitudes are responses of the rotational system to higher-frequency forcing (the Chandler at 433 d, the annual at 365 d) and are determined by the transfer function at those frequencies, not by secular mass redistribution. The 98.3 per cent reduction in Chandler amplitude and

97.2 per cent reduction in annual amplitude over the same epoch in which the mean-pole drift accelerated are not predicted by mass-loading models.

Second, mass-loading mechanisms do not degrade η as defined and measured in Paper III. The transfer-function inversion uses GFZ AAM/OAM/HAM forcing series as the input and the IERS pole response as the output; the ratio at fixed frequency is independent of any secular mass-distribution change that does not enter the forcing or response timeseries at the test frequencies. The 45-fold decline in η reported in Paper III is a transfer-function failure, not a forcing or mass redistribution.

Third, the directional convergence at 75°W documented by Paper II's five independent methods is not predicted by mass loading. The bearings of pole drift driven by Greenland, WAIS, and AIS mass loss are each different and individually documented in the literature (Adhikari & Ivins 2016, Figure 3); the LLSVP gravitational perpendicular at 75°W is not the prediction of any individual ice sheet contribution. The fact that the empirical convergence aligns with the LLSVP-tensor-derived perpendicular rather than with any single ice-sheet bearing is the directional discriminator.

What the present paper does not do is execute the per-component decomposition that would subtract a GRACE-derived mass-loading contribution from the mean-pole drift series and examine the residual. Such an analysis is the natural next refinement; the expectation, given that Paper II's bearing convergence already includes a GRACE mass-centroid method as one of its five converging streams (Paper II Section 5), is that the residual would still align with the 75°W bearing. We flag this as future work and note that the central argument of this paper does not depend on its outcome, it depends on the joint behaviour of the four observational streams, three of which are not mass-loading observables at all.

4.5 What is not claimed

This paper does not claim that a transition between basins is imminent, nor that its timing is predictable within this analysis, nor that the pole must complete the migration along the trajectory it has thus far traced. The arc distance from State 1 to State 2 is derived in Paper V; its dynamical realisation, and the timescales thereof, are the subject of Paper VI. What is claimed here is that State 2 exists as a directional feature of the present-day rotational state space, that the pole has demonstrably begun responding to the gravitational forcing directed toward it, and that the coupling regime documented in Paper III places the system outside the parameter space in which the quasi-fluid TPW framework is defined. These claims are independently verifiable against the IERS EOP record, the seismic tomography consensus, and the data products cited in Papers I through III.

5 CONCLUSIONS

Monte Carlo diagonalisation of the combined African-plus-Pacific LLSVP inertia tensor at 10^6 samples per province averaged across 20 independent seeds establishes that the LLSVP mass distribution produces off-diagonal inertia components directed along a specific geographic bearing, identifying a second principal-axis equilibrium (State 2) along that direction. The result is robust across four published tomographic reconstructions. Paper II's convergent evidence from five independent methods (velocity-cusp at 72.8° ± 0.6°, LLSVP geometric at 80° ± 15°, curvature blind search at 79°, GRACE mass centroid, plus curvature-cusp detection) places the five-method mean forcing bearing at 75.4° ± 3.4° in pole-plane coordinates at R = 0.9982, corresponding to approximately 75°W in geographic azimuth. The 5-year mean pole position computed from the IERS EOP 20 C04 record (1962–2026) shows monotonic outward migration from 228 mas in 1970–1975 to 394 mas in 2025–2026, a 73 per cent increase, with 87 per cent of the total displacement aligned to the 75°W attractor direction. The mean pole crossed the attractor great circle during the 2010–2015 window and has migrated beyond it through 2025–2026. Taken together with the wobble collapse (Paper I), the cusp-bearing convergence (Paper II), and the coupling collapse (Paper III), these results establish Earth's rotational multi-stability as an observationally supported feature of the present-day geodynamic state. The arc distance from State 1 to

State 2 and the specific geographic coordinates of State 2 are derived in Paper V of this series from the Outer Rotating Body inertia tensor and Euler-equation integration; the question of whether the present migration trajectory presages a complete transition on an observable timescale is addressed in Paper VI.

DATA AVAILABILITY

IERS EOP 20 C04 pole coordinates are available from https://hpiers.obspm.fr/iers/eop/eopc04/. Seismic tomography models S40RTS (Ritsema et al. 2011) and SEMUCB-WM1 (French & Romanowicz 2015) are available from the IRIS Data Management Center. The S40RTS netCDF grid used for the field integration of Section 3.5 is distributed at https://github.com/shuleyu/seismic-tomography-models (S40RTS_dvs.nc). GEOSYNC Monitor operational pole migration visualisations are available at https://geosyncmonitor.com. Analysis code developed for this analysis, including the ORB-tensor cap construction (orb_tensor.py, tomography_variants.py, iitpw_solver.py) and the S40RTS field-integration routine (orb_tensor_field.py), is available upon request to the corresponding author.

REFERENCES

Adhikari S., Ivins E.R., 2016. Climate-driven polar motion: 2003–2015. Sci. Adv., 2, e1501693.

Bizouard C., Lambert S., Gattano C., Becker O., Richard J.-Y., 2020. The IERS EOP 14 C04 solution for Earth orientation parameters consistent with ITRF 2014. J. Geod., 93, 621–633.

Chandler S.C., 1891. On the variation of latitude. Astron. J., 11, 59–61.

Chen J.L., Wilson C.R., Ries J.C., Tapley B.D., 2013. Rapid ice melting drives Earth's pole to the east. Geophys. Res. Lett., 40, 2625–2630.

Cottaar S., Lekić V., 2016. Morphology of seismically slow lower-mantle structures. Geophys. J. Int., 207, 1122–1136.

Dziewonski A.M., Hager B.H., O'Connell R.J., 1977. Large-scale heterogeneities in the lower mantle. J. geophys. Res., 82, 239–255.

French S.W., Romanowicz B., 2015. Broad plumes rooted at the base of the Earth's mantle beneath major hotspots. Nature, 525, 95–99.

Goldreich P., Toomre A., 1969. Some remarks on polar wandering. J. geophys. Res., 74, 2555–2567.

Gross R.S., 2015. Earth rotation variations — long period. In: Treatise on Geophysics (ed. G. Schubert), 2nd edition, vol. 3, 215–261. Elsevier.

Karato S., Karki B.B., 2001. Origin of lateral variation of seismic wave velocities and density in the deep mantle. J. geophys. Res., 106, 21771–21783.

Kirschvink J.L., Ripperdan R.L., Evans D.A., 1997. Evidence for a large-scale reorganization of Early Cambrian continental masses by inertial interchange true polar wander. Science, 277, 541–545.

Koelemeijer P., Deuss A., Ritsema J., 2017. Density structure of Earth's lowermost mantle from Stoneley mode splitting observations. Nat. Commun., 8, 15241.

Kuang W., Chao B.F., Chen J., 2019. Decadal polar motion of the Earth excited by the convective outer core from geodynamo simulations. J. geophys. Res. Solid Earth, 124, 10,288–10,307.

Matsuyama I., Mitrovica J.X., Manga M., Perron J.T., Richards M.A., 2006. Rotational stability of dynamic planets with elastic lithospheres. J. geophys. Res., 111, E02003.

McNamara A.K., Zhong S., 2005. Thermochemical structures beneath Africa and the Pacific Ocean. Nature, 437, 1136–1139.

Mitrovica J.X., Wahr J., Matsuyama I., Paulson A., 2005. The rotational stability of an ice-age Earth. Geophys. J. Int., 161, 491–506.

Mitrovica J.X., Hay C.C., Morrow E., Kopp R.E., Dumberry M., Stanley S., 2015. Reconciling past changes in Earth's rotation with 20th century global sea-level rise. Sci. Adv., 1, e1500679.

Ricard Y., Spada G., Sabadini R., 1993. Polar wandering of a dynamic Earth. Geophys. J. Int., 113, 284–298.

Ritsema J., Deuss A., van Heijst H.J., Woodhouse J.H., 2011. S40RTS: a degree-40 shear-velocity model for the mantle from new Rayleigh wave dispersion, teleseismic traveltime and normal-mode splitting function measurements. Geophys. J. Int., 184, 1223–1236.

Spada G., Ricard Y., Sabadini R., 1992. Excitation of true polar wander by subduction. Nature, 360, 452–454.

Steinberger B., Torsvik T.H., 2010. Toward an explanation for the present and past locations of the poles. Geochem. Geophys. Geosyst., 11, Q06W06.

Steinberger B., Seidel M.-L., Torsvik T.H., 2017. Limited true polar wander as evidence that Earth's nonhydrostatic shape is persistently triaxial. Geophys. Res. Lett., 44, 827–834.

Torsvik T.H., Steinberger B., Gurnis M., Gaina C., 2012. Plate tectonics and net lithosphere rotation over the past 150 My. Earth planet. Sci. Lett., 291, 106–112.

Torsvik T.H., van der Voo R., Doubrovine P.V., Burke K., Steinberger B., Ashwal L.D., Trønnes R.G., Webb S.J., Bull A.L., 2014. Deep mantle structure as a reference frame for movements in and on the Earth. Proc. Natl. Acad. Sci. USA, 111, 8735–8740.

Tsai V.C., Stevenson D.J., 2007. Theoretical constraints on true polar wander. J. geophys. Res., 112, B05415.

Vaes B., van Hinsbergen D.J.J., Boschman L.M., 2025. Slow true polar wander around varying equatorial axes since 320 Ma. AGU Advances, 6, e2024AV001515.

Yuan Q., Li M., 2022. Instability of the African large low-shear-wave-velocity province due to its low intrinsic density. Nature Geoscience, 15, 334–339.

Zacharias, 2026a. Unprecedented extinction of Earth's Chandler and annual wobbles: evidence for degraded core-mantle boundary coupling (1846–2026). Manuscript in preparation (Paper I of this series).

Zacharias, 2026b. Systematic directional forcing of Earth's rotation pole toward 75°W: convergent evidence from polar motion cusps, satellite gravimetry and geomagnetic field correlation (1973–2026). Manuscript in preparation (Paper II of this series).

Zacharias, 2026c. Critical degradation of Earth's rotational coupling revealed by transfer function inversion and broadband polar motion analysis (1973–2026). Manuscript in preparation (Paper III of this series).

Zacharias, 2026e. Derivation of the post-transition rotational equilibrium axis from the Outer Rotating Body inertia tensor and Paper II forcing direction. Manuscript in preparation (Paper V of this series).